Chapter 3.11

Mechanical stability of fast hard X-ray spectroscopy beamlines

Klaus Attenkofer*

ALBA Synchrotron, Carrer de la Llum 2-26, 08290 Cerdanyola del Vallès, Barcelona, Spain. *Correspondence e-mail: kattenkofer@cells.es

This chapter presents a summary of fast or quick EXAFS beamlines and monochromation, including how to improve the energy stability and precision so as to collect a single nonrepeated full EXAFS spectrum in a time of the order of seconds or milliseconds, with point integration times on a continuous scan of the order of 0.1 ms or 1 µs. This is based around 1000 points per continuous scan and requires high fluxes on sample. Typical energy ranges are for K edges in the harder X-ray regime, for example 7–30 keV.

1. Introduction

Driven by the needs of *operando* and *in situ* experiments, nearly every facility has developed beamline concepts which allow data acquisition of full spectra of the order of seconds to milliseconds. Besides dispersive extended X-ray absorption fine structure (EXAFS) instruments (Mairs *et al.*, 2010; Gaur *et al.*, 2013; Pellicer-Porres *et al.*, 1998), based on a single-shot strategy which uses a polychromatic approach of focusing rays of all energies on the sample position and using a photon energy–spatial correlation past the focus position to determine the absorption spectrum, most facilities use fast-scanning double-crystal monochromator beamlines, often called quick EXAFS (QEXAFS) beamlines (Müller *et al.*, 2016; Dent *et al.*, 2009; Prestipino *et al.*, 2011; Khalid *et al.*, 2010; Frahm *et al.*, 2010; Solé *et al.*, 1999). These fast-scanning beamlines, which not only offer the capability of fast scanning via continuous scan technology but also provide sufficient photon flux to collect the necessary photon statistics in a single scan, are of increasing importance for *operando* optimized or high-throughput beamlines.

2. General considerations

In this article, we will discuss the specific stability requirements that enable a successful and user-friendly program at these beamlines. From the perspective of the hardware, three different time scales can be distinguished with respect to beam-position motion and energy stability: (i) a fast regime from picoseconds to milliseconds, which is mainly determined by electron-ring dynamics and electron-beam stability, (ii) the millisecond to second range, which is mainly dependent on mechanical vibrations of the beamline and ring components, and (iii) long-term drifts from seconds to weeks or even months that are correlated with thermal and other long-term effects, such as ground motion or deformations due to vacuum forces.

Based on the details of the optics, motion and vibrations of the source point or individual optics components may either

Table 1
Heat loads on the high heat-load components of the ISS beamline at NSLS-II.

For each of the modes the total power loss of each optical element is compared with the three loss channels (Thomson scattering, Compton scattering and absorption). The last column gives the full power transmitted through the element.

Energy mode	Component	Total power loss (W)	Thomson scattering (W)	Compton scattering (W)	Photoabsorption (W)	Transmitted power (W)
DW100 1.1 mrad × 0.1 mrad				5698		
Low	C 25 μm	351	5	5	340	5347
	First mirror (Si)	3118	357	230	2531	2229
	Second mirror (Rh)	201	3	6	192	2027
	First monochromator crystal	2027	6	31	1989	—
Medium	C 1550 μm	2072	108	193	1772	3626
	First mirror (Rh)	1145	114	253	778	2481
	Second mirror (Rh)	281	20	22	239	2200
	First monochromator crystal	2200	96	60	2044	—
High	C 5600 μm	2849	186	385	2278	2849
	First mirror (Pt)	776	75	188	513	2073
	Second mirror (Rh)	313	22	29	261	1760
	First monochromator crystal	1760	106	98	1556	—

impact the delivered photon energy, the beam position, the beam shape and size, the higher harmonic contribution or a combination of all of these properties. A broadening of the individual quantity is the consequence of drifts and vibrations with dynamics significantly faster than the integration time of an individual data point. Depending on the homogeneity of the sample and the detection method, motion comparable to the integration time results in noisy spectra, while long-term drifts with time scales significantly longer than the integration time result in various systematic errors, including edge shifts between scans and deformations of the observed spectra due to changing sample thickness and higher harmonic contributions.

The integration time of the individual data point depends on the details of the data-acquisition strategy, for example the details of the monochromator acceleration profile and the interpolation algorithm calculating the detector signals on the desired energy grid; for a 1 s scan this integration time is typically of the order of 0.1 ms, allowing an oversampling of at least a factor of ten. For faster scan speeds the integration time can easily reach 1 μs and even below.

Very little work has so far been performed to measure the impact of electron-beam instabilities and other fast variations of the source on the energy resolution or beam size. Especially for wiggler beamlines with relatively large, homogeneous and divergent X-ray beams, other effects such as heat load-related deformations of the optics are far more important (Bilderback et al., 1986; Proux et al., 2006), making a quantitative correlation of beam dynamics and beamline performance extremely difficult. This leaves the variations in the intermediate time scales in the range of milliseconds and the long-term drifts as the dominant factors causing deterioration of the statistical data quality.

Mechanical vibrations of the optics are typically the dominant factor for motions and intensity changes in the millisecond range, even if beam-relaxation effects during the top-up injections and electron-beam motions caused by the fast feedback system of the accelerator can influence the noise behaviour. With the increased electron-beam stability available at modern storage rings, thermal drifts of the optics are the main contributors to long-term drifts in high heat-load beamlines.

To estimate the heat load and the required flux for a single EXAFS scan performed in one second, we want to discuss a typical catalysis experiment with an atomic concentration of the catalytic material of about 1%. Depending on the applied detection method, for example total fluorescence or energy-discriminating detection, the required statistical error is between 10^{-3} and 10^{-4} per point. Assuming about 1000 points per scan and due to limited solid-angle coverage and/or filter and X-ray optics losses, a detection efficiency of about 1% and the absorption of 90% of the photons by the substrate, the beamline will need to provide between 10^{12} and 10^{14} photons s^{-1} on the sample. Such a flux is achieved on high-flux beamlines using either undulator or wiggler insertion devices as sources. In both cases the beamline components are exposed to a significant total heat load of thousands of watts and a power density of hundreds of W mm^{-2}, making efficient thermal management essential (Yang et al., 2010).

The thermal management of white-beam and pink-beam components should not only address the cooling requirements of the optics itself, which are necessary to ensure the optical specifications, but also tackle secondary effects caused by scattered X-rays from the optical component causing local heating of support structures and ultimately mechanical long-term drifts. Table 1 shows the power dissipations of individual components due to absorption, Thomson and Compton scattering for the example of a damping wiggler beamline at NSLS-II. The scattered light can easily sum to hundreds of watts, resulting in significant heating if not shielded; additionally, it will result in damage to wiring, thermocouples and encoders in the long run.

The ratio between absorption, Compton and Thomson scattering depends on the electron density of the optical component, the spectral contribution of the X-rays and the geometry of the component (Kirz, 2009). A detailed simulation is necessary to determine appropriate cooling for the individual optics component and its surrounding shielding.

358   Klaus Attenkofer • Fast hard X-ray spectroscopy beamlines

Int. Tables Crystallogr. I (2024). ch. 3.11, 357–364

The Compton-scattered intensity distribution can easily be calculated following the Klein–Nishina formula (Klein & Nishina, 1929), but can typically be expected to be isotropic if the critical energy of the source is below 20 keV (Hamzawy, 2016; Akhavan & Vosoughi, 2015). For very hard sources such as some superconductive wigglers or high-energy rings the forward-scattering direction will be enhanced.

The calculation of the distribution function of Thomson-scattered photons is significantly more difficult when the optics are made from single-crystal material. In this case, Bragg scattering will create hot spots which are difficult to predict and shield, since their appearance depends on the exact orientation of the optical element. In most cases, the X-ray beam has to penetrate significant amount of materials of the order of centimetres or even tens of centimetres inside the optics; as a consequence, only photons of 40 keV and higher will play a significant role. For hard X-ray sources, these Bragg-scattered photons result in localized areas of the size of the X-ray beam being heated; they can result in extreme local heating if the absorbing material has a low thermal conductivity or is otherwise thermally insulated.

3. Mirror systems

The need to manage the heat load and to minimize the mechanical vibrations drives most of the design decisions for the beamline layout and beamline components. In the following section, the Inner Shell Spectroscopy (ISS) beamline, a high-flux spectroscopy beamline at NSLS-II, will be used to show typical technical solutions. The ISS beamline uses a damping wiggler source (Leshchev *et al.*, 2022) with an acceptance angle of 1 mrad horizontal and 100 µrad vertical, resulting in a flux of 10^{13} and 10^{14} photons s^{-1} at the sample position, a beam size of 500×500 µm and an energy range of 4.7–36 keV. With a heat load of nearly 5.7 kW at the first optical component, the beamline shows all of the typical features of state-of-the-art high-flux EXAFS beamlines. To allow user-friendly operations and minimize higher harmonic spectral contributions, the beamline is operated in three different configurations providing a low-energy range from 4.7 to 13 keV, a medium-energy mode from 12 to 23 keV and a high-energy mode from 16 to 36 keV.

After the frontend, which contains the white-beam slits, the white beam is tailored to one of three energy ranges by the use of a high-pass filter consisting of pyrolytic graphite filters of various thicknesses and a low-pass filter effected by a high heat-load mirror: a 1.5 m long direct-cooled mirror with silicon, rhodium and platinum coatings. The band pass is optimized for the three different operation modes by changing the thickness of the graphite filter and the mirror coating by horizontal translation of the mirror. This band-pass filter system is followed by a collimation mirror and finally by the high heat-load monochromator using a pseudo-channel-cut Si(111) direct-driven monochromator. The achieved collimation is matched to the rocking-curve width of a Si(111) crystal and depends on the thermal deformations of the high heat-load mirror; it ranges from about 7 µrad in the low-energy

mode to 3 µrad in the medium-energy and high-energy modes. The monochromator is followed by a second, optional high-resolution Si(220) channel-cut monochromator. When used, the four crystals of the two monochromators are arranged in a −++− geometry (DuMond, 1937), forming a true four-crystal monochromator system. The monochromatic beam is focused by one of two 1.5 m long toroidal mirrors coated with platinum and rhodium. The centre of the focusing system is located 36.9 m downstream from the centre of the straight section and 32.0 m upstream from the sample position. A higher harmonic rejection mirror system is installed as the last optical element about 6 m upstream from the sample position following the beam-defining sample-slit system.

Most modern high-flux EXAFS beamlines follow a similar layout, with a total length of 50–70 m (Simonelli *et al.*, 2016; Klementiev *et al.*, 2016; Diaz-Moreno *et al.*, 2018; Jiang *et al.*, 2007). A simplification can be achieved by eliminating the high-resolution monochromator. In the case of a more moderate heat load, the high heat-load mirror and the collimation mirror can be combined using a single-mirror system. Reducing the construction costs, a single-mirror high heat-load collimation system has two significant disadvantages: the mirror bender has to be combined with an efficient cooling scheme and the mirror system has to tolerate a large fluctuation in heat load depending on the energy range (see Table 1). This makes adjustment of the collimation over the energy range necessary, which significantly complicates the operations of the beamline.

The relatively large number of optical elements (of the order of three to four mirror systems) and the large distance of the mirrors and monochromator(s) from the sample position require specific care to minimize any vibrations or drifts in the scattering plane of the optics. A vibration or a drift with 1 µrad amplitude from a mirror or monochromator at a 30 m distance will result in a 60 µm beam motion, which is roughly 10% of the typical beam size. This example demonstrates the stiffness and precision which need to be achieved; it is especially challenging to accomplish long-term stability, which will ultimately determine the user-friendliness and the productivity of the beamline.

To obtain mechanical and thermal stability, most modern mirror systems completely decouple the mirror mount and mechanics from the vacuum tank. The mechanics are typically built on a large granite block, providing minimal thermal expansion and damping of mechanical vibrations. Various mechanics can be found, including hexapods and other trisphere systems. In each of these cases a careful vibration and thermal analysis is required to ensure the required precision. As shown in Fig. 1, ISS uses conventional kinematic tables with three vertical motions mounted outside the vacuum. To minimize vibrations and thermal drift, the mechanics include large vertical wedge stages, table plates made from granite and vertical elements made from stainless steel. Analyzing the eigenmodes of the granite plates and the system in total allowed a geometry with a minimum vibrational amplitude within the scattering plane of the mirrors to be chosen. Using a single block of granite as a base for both

mirror systems and the beam-defining masks and collimators guarantees long-term stability of the alignment by minimizing the effects of seasonal floor motions.

The vertically deflecting mirror system itself, shown in Fig. 2, integrates all beam-defining masks and various shields to minimize the risk of damaging the system by mis-steering the pink beam and to handle the scattered photons from the individual components. To avoid any exposure of the collimation mirror, its mount and its bender, the high heat-load mirror is fully encapsulated by a 3 mm water-cooled copper shield. In addition, a mask directly mounted downstream of the high heat-load mirror, in combination with a 20 mm thick tungsten shield, protects the collimation mirror system from any forward-scattered photons. The support plate of the mirror and the interface plate hosting the in-vacuum horizontal motion system are made of 25 mm high-strength aluminium plates, providing high thermal conductivity and low absorption probability for highly energetic photons, resulting in minimal thermal drifts owing to down-reflected Bragg-scattered photons. The 20 mm thick stainless-steel vacuum tank, which is not shown in Fig. 2, provides additional shielding of the out-of-vacuum mechanics.

The collimation mirror with its bender is one of the optical elements which has the highest impact on the spectral quality of the beamline. Its positioning, cooling and bending not only define the final beam position and shape, but also impact the energy resolution of the beamline. In collaboration with the vendor, TOYAMA, we developed a symmetric piezo bender with integrated load cell to provide a quantitative measure of the bending force of the mirror.

The mirror cage is built from high-strength aluminium with integrated water-cooled copper plates to achieve the fastest thermalization and high thermal stability. Using finite-element analysis, the indirect cooling geometry of the mirror and the heat transport through the mirror-mounting points was optimized, resulting in a usable length of 1.45 m. The thick copper cooling plates used for indirect cooling of the mirror also provide shielding of the sensitive bender mechanism. The side
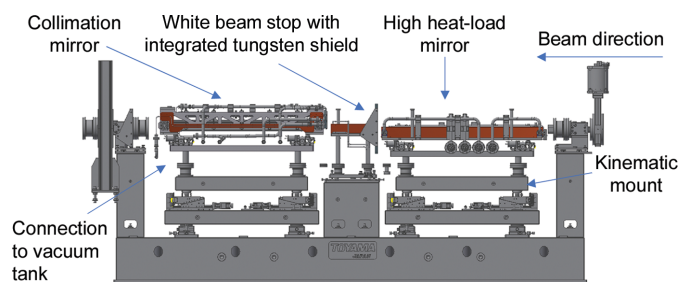
copper cooling plates are also thermally coupled to the mounting point of the gravity compensation of the mirror, which is essential for long mirrors. Finite-element analysis showed that temperature control of the gravity compensation is essential to keep the figure errors of the mirror below 1.5 µrad.

With a total power loss of more than 3 kW, water cooling of the system requires a significant flow rate of up to $20\,\text{l}\,\text{min}^{-1}$ in the individual cooling circuits. To avoid turbulence inside the cooling lines, all movable connections are made with smooth supported silicon tubing surrounded by bellows which provide the necessary vacuum guard. Additional efforts were made to minimize any turbulence by avoiding strong curvatures of the feed and return lines to the heat exchanger, which decouples the mirror cooling water from the chilled water of the facility. The decoupling provides the ability to control the water chemistry of the cooling water and allows the feed pressure, return pressure and temperature of the cooling water to be tuned.

4. Monochromator

The heart and the key component of any spectroscopic beamline is the monochromator. It presents the highest technical challenges to satisfy high positioning precision for fast-scanning parts under high cooling requirements, and due to its fast-scanning requirements it is also specific to spectroscopic beamlines and therefore has been developed by a relatively small subset of X-ray users. Over the past decade direct-drive monochromators have been developed, and are now the gold standard for fast-scanning monochromators (Müller *et al.*, 2015; Kristiansen *et al.*, 2015; Kelly *et al.*, 2013; Busetto *et al.*, 1995). In contrast to conventional monochromators, which use a turntable driven by a worm gear or couple the motor drive via some type of gear with a high gear ratio, direct-drive monochromators have only a single movable axis which directly connects the motor to the turntable.
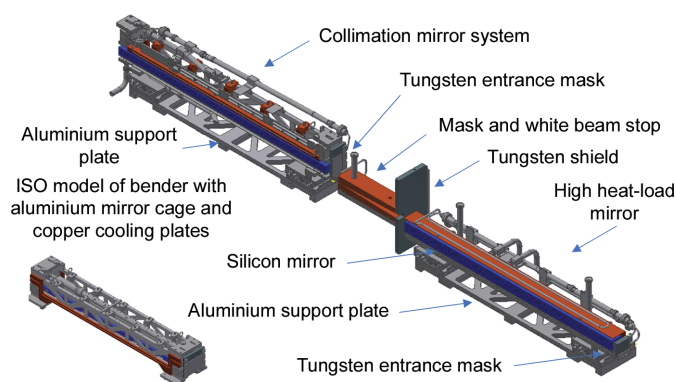

Figure 1
ISS collimation mirror system containing the high heat-load mirror, the collimation mirror and various masks, collimators and secondary *Bremsstrahlung* shielding elements. To allow long-term alignment stability of all components, the system is built on a large 4.5 m long granite block. The motion system of each mirror is fully decoupled from the vacuum tank and uses three independent external vertical stages forming a kinematic motion system. Radiation-shielding elements around and between the mirrors protect the mechanical components and encoders from Thomson and Compton scattering and *Bremsstrahlung*.

Figure 2
Cut through the collimation mirror system with its shielding and heat-management system. All water-cooled copper elements are shown in red, silicon mirrors in blue and tungsten shielding elements in dark grey. All other high-strength aluminium structural elements are shown in light grey. An ISO model of the collimation mirror with bender is shown in the left corner. The aluminium cage structure in combination with actively cooled copper plates allows fast thermalization and stable working conditions of the collimation mirror.

The progress in control and encoder technology has made this technology standard and allows measurements that are fast and at the same time precise. The ISS high heat-load monochromator has an encoder resolution of 50 nrad and updates the position at 10 MHz. This allows the monochromator to routinely be run with a 500 nrad follow error tolerance. In contrast to other methods, which allow only sine-wave motions (Frahm *et al.*, 2010; Jiang *et al.*, 2007), the ISS concept allows any arbitrary motion to be programmed using a predefined position table, the so-called trajectory. The trajectory is calculated with a point density of 16 000 points per second, uploaded into the memory of the motor controller and executed for each scan. Optimizing the trajectory by avoiding sudden changes in acceleration is essential to minimize vibrations between the first and second monochromator crystal, ultimately resulting in noise-free spectra and position-stable beams.

Most fast-scanning monochromators use water-cooled channel-cut monochromators (Busetto *et al.*, 1995; Müller *et al.*, 2016; Stötzel *et al.*, 2008; Khalid *et al.*, 2010; Frahm *et al.*, 2005). These systems have the advantage that the first and second crystals are manufactured from the same silicon block with a solid-state flexure connecting the two crystals that allows detuning of the system. The resonance frequency for vibrations between the first and second crystals can easily be tuned to the 500–800 Hz regime, making these monochromators very stable. In addition, they have a low weight, allowing a relatively small drive system with low inertia (http://idtnet.co.uk/downloads/IDT_product_guide.pdf; Zhang *et al.*, 2003; Frahm *et al.*, 2004).

Using a more complex indirect liquid-nitrogen cooling system, the channel-cut version can be used up to a heat load of 500–700 W (Chumakov *et al.*, 2004; Zhang *et al.*, 2003), depending on the power density of the beamline. In the case of ISS, the monochromator is designed for a heat load of up to 2.2 kW. This heat load requires a direct-cooled first crystal assembly and the use of a pseudo-channel-cut system, making the turntable assembly significantly heavier. The need for additional alignment mechanics between the two crystals brings additional risks of low-frequency vibrations which will impact the observed noise behaviour of the spectra.

To avoid these issues, the monochromator assembly, shown in Fig. 3, is built with a minimal number of mechanical degrees of freedom; in addition, the individual motion stages are optimized for stiffness, pushing the resonance frequencies above 50 Hz. To minimize the moment of inertia, the design was optimized by mounting all of the heavy equipment as close to the rotation axis as possible. A stainless-steel, thick-wall tubing with a total weight of 90 kg was used as a rotor axis combining the turntable assembly with the motor. The full assembly, including the turntable and both crystal mounts, weighs 250 kg; a 2.6 kW motor maximally achieves a 10 Hz oscillation of this structure for a typical 1.5 keV long EXAFS scan. The maximal deformation of the rotor during maximal acceleration is smaller than 100 nrad. Using a massive steel construction, the full monochromator is mounted on a solid granite block, avoiding vibrations of the structure excited by the scan motion. The total weight of the monochromator unit as shown in Fig. 3 is about 8 tons.

The full rotor and turntable assembly with mounting block is shown in Fig. 4. An important detail of the design is the on-axis feed of the cooling lines. In this arrangement no forces are transferred from pressure variations in the feed and return lines, resulting in a smooth motor motion, ensuring easy tuning of the motor driver. By using a pigtail design for the cooling lines in combination with a large-volume insulation vacuum chamber, vibrations of the feed lines are minimized.

The minimized vibrations in the feed line in combination with the use of ferrofluidic feedthroughs instead of differentially pumped elastomer feedthroughs result in a long lifetime of the monochromator with long service intervals for the mechanics. The lifetime expectation of the current design is ten years.

The cooling of the first crystal is a specific challenge for high-flux beamlines. Besides the issue of exceptionally high
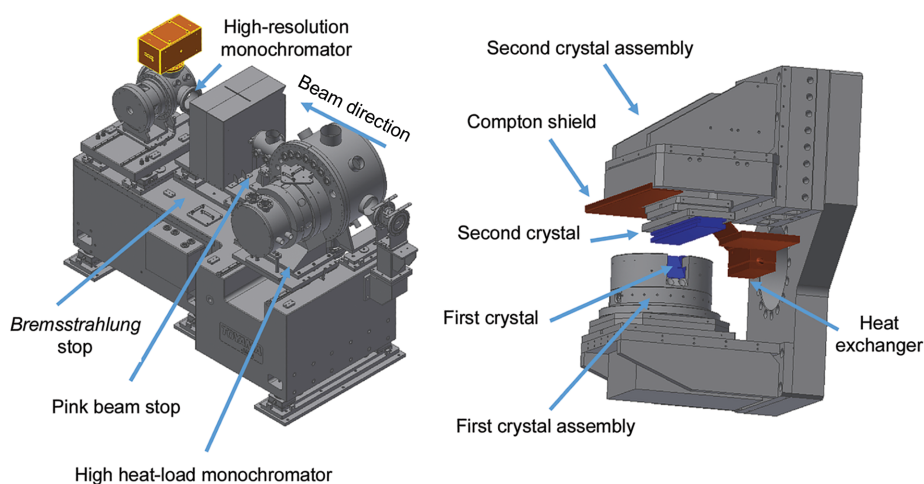

Figure 3
ISS monochromator assembly (left) including high heat-load monochromator, pink-beam stop, *Bremsstrahlung* stop and high-resolution monochromator. The turntable assembly (right) shows the first crystal mount, the second crystal mount with piezo motor assembly and the heat exchanger cooling the Compton shield and the second crystal.

cooling power requirements, requiring improved heat-exchange designs, the high flow rate of liquid nitrogen and the risk of bubble formation creates a high risk of vibrations and intermittent forces on the rotation axis, resulting in challenging tuning of the direct-drive system. At ISS, the necessary cooling is provided by a $20\,l\,min^{-1}$ liquid-nitrogen flow through the crystal. A classical hockey-puck cooling design was combined with a stainless-steel liquid guide plate which interlinks with the silicon cooling fins, creating 20 cooling channels with a cross section of about 500×9 mm (see Fig. 4). This novel high-impedance heat-exchanger concept in combination with an improved standard liquid-nitrogen pump allows a 3 bar pressure drop to be created over the crystal assembly and a laminar flow in the channel with a high flow velocity (between 3.1 and $3.7\,m\,s^{-1}$). The high flow velocity provides the necessary cooling power and allows any bubbles formed at the silicon–liquid nitrogen interface to be removed easily and rapidly, avoiding intermittent cooling loss.

This arrangement provides sufficient cooling to the first crystal that the surface temperature is above 125 K and reaches a maximum of 140 K. The resulting maximal slope error is typically 20 µrad; however, most of the slope error can be described by a cylindrical distortion which is corrected by adjustment of the bending of the radius collimation mirror. According to the results of finite-element analysis combined with ray-tracing and metrology results for the mirrors, the resulting slope error is of the order of 5 µrad. This slope-error calculation assumes the full beam size.

An additional source of instability can be identified if the surface temperature is close to the zero thermal expansion point; depending on the purity of the silicon, this critical temperature is around 115 K (Rogers & Assoufid, 1995; Zhang *et al.*, 2013). The thermal expansion coefficient is negative and its derivative is positive, resulting in a contraction of the material on an increase in temperature in the temperature range between 80 K and the zero thermal expansion point (White, 1973). This effect results in a negative 'thermal bump' (Zhang *et al.*, 2013). For temperatures above the zero thermal expansion point, the thermal expansion coefficient and its derivative are positive, resulting in an expansion with temperature increase. In this case one observes a positive 'thermal bump' (Zhang *et al.*, 2013). In both cases the resulting shape error can approximately be described by a cylindrical error which can be compensated by the collimation mirror system. A complex deformation develops in the intermittent temperature range, in which parts of the illuminated area are below and others are above the zero thermal expansion point (Zhang *et al.*, 2013). The resulting deformations cannot be corrected in this case; for wiggler sources with a significant footprint on the crystal, the resulting shape errors reach tens of microradians, producing a complex optical response function which depends on the rocking-curve width of the chosen reflection relative to the shape error. Observable effects are spoiled energy resolution, aberration errors of the focus and beam-intensity variations in the focal spot. Caused by the rotation of the crystal during the scan, the illuminated footprint varies, creating variations of the temperature conditions and therefore resulting in a complex variation of the beam behaviour at the sample position.

5. Energy stability

A series of transmission XAFS experiments were performed on gold samples to test the energy stability of the beamline and to demonstrate that the beamline can perform absolute absorption measurements. Using 60 and 40 nm thick gold films sputtered on a Kapton membrane, the L_3 edge of gold including the EXAFS range up to the L_2 edge was measured. A 30 s scan length was chosen for all measurements and the scans were repeated within a time span of 150 min. The measurements were performed at the end of the commissioning time, about 15 months after the first X-rays were detected in the end station.

To determine the energy calibration of each scan, the first derivative of each scan was calculated and the pulse shape around the maximum was fitted with a Gaussian-shaped profile. The Gaussian shape does not perfectly describe the asymmetric shape of the measured feature, but the absolute error between the measurements is constant since the signal shape does not change from measurement to measurement. An example of this approach is shown in Fig. 5. Using this approach, the point density of the spectrum and the statistical noise of each point plays a reduced importance, allowing the energy position to be determined with millielectronvolt level precision.

Fig. 6 shows the time evolution of the energy calibration from all measurements of the 60 nm thick sample. The standard deviation σ of this data set is 30 meV. The plot shows a scattered plot with no tendency to systematic long-term drift, indicating that at least part of the standard deviation is caused by the statistical error of determining the energy calibration of
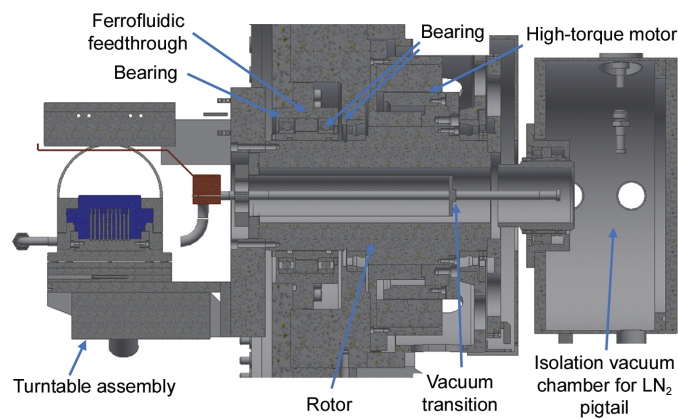

Figure 4
Cross section of the ISS high heat-load monochromator. A massive 90 kg rotor supports the high-torque motor and the turntable assembly. The liquid-nitrogen feed and return lines are guided in the middle of the rotor, reducing forces on the rotation axis due to differential pressure in the two lines. The separation of the monochromator UHV and the isolation vacuum for the liquid-nitrogen support is located in the middle of the rotor axis. The total weight of the rotor and turntable assembly is approximately 250 kg.
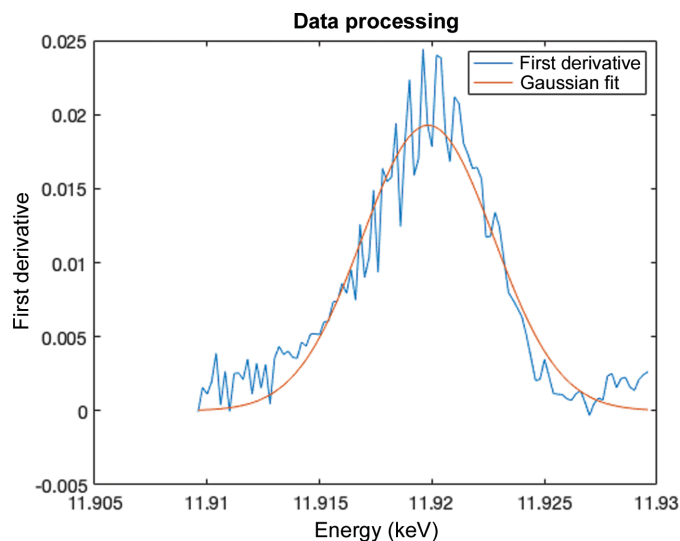
Figure 5
First derivative of the absorption spectrum from a 60 nm thick gold film sputtered onto a Kapton membrane. The plot shows the comparison between a Gaussian fit and the enlarged area of the first derivative of the absorption spectrum.
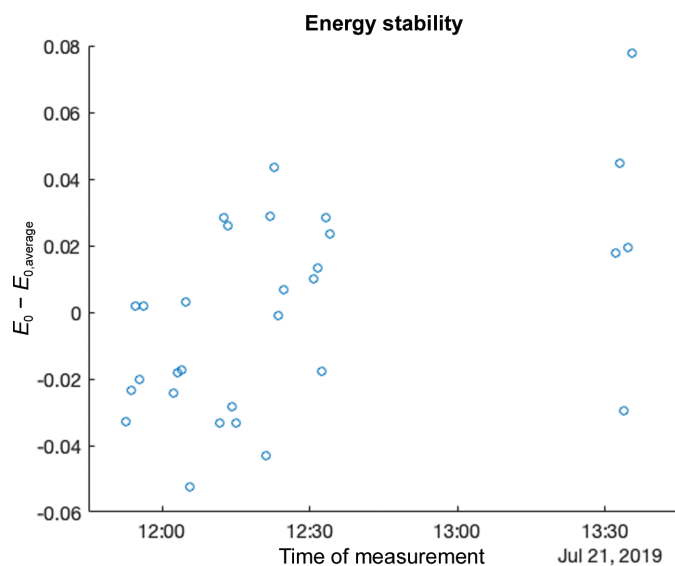

Figure 6
Energy calibration variation over time. The variation is plotted in eV. The statistical variance of the measured points is 30 meV.

the individual scan. Using a 2σ requirement the energy drift is approximately 60 meV; *i.e.* there is a 95% probability that the measured energy is within the 60 meV energy window. This result is consistent with experiences during the operation of the beamline.

6. Conclusions

The 18-month operation experience of ISS has shown that a user-friendly, stable, high-flux beamline can be built and operated. With 52 user publications in this period, ISS is currently one of the most successful beamlines at NSLS-II. Under normal operation conditions, the beamline has a 'warm-up' time of approximately 5 min, *i.e.* the waiting time after which the beamline can be operated without additional alignment followed by beam-loss recovery. Typical energy drifts of the monochromator over 24 h are below 50 meV. The flux of 10^{14} photons s^{-1} on the sample typically allows data acquisition to take place within a minute for a given sample condition, even if the sample or the reactor is not fully optimized for X-ray experiments. Equally important to the high beam intensity at the sample position is the user-friendly change of energy range for high-throughput operation of the beamline.

References

Akhavan, A. & Vosoughi, N. (2015). *Radiat. Phys. Chem.* **117**, 160–166.

Bilderback, D. H., Mills, D. M., Batterman, B. W. & Henderson, C. (1986). *Nucl. Instrum. Methods Phys. Res. A*, **246**, 428–433

Busetto, E., Lausi, A. & Bernstorff, S. (1995). *Rev. Sci. Instrum.* **66**, 2078–2081.

Chumakov, A., Rüffer, R., Leupold, O., Celse, J.-P., Martel, K., Rossat, M. & Lee, W.-K. (2004). *J. Synchrotron Rad.* **11**, 132–141.

Dent, A. J., Cibin, G., Ramos, S., Smith, A. D., Scott, S. M., Varandas, L., Pearson, M. R., Krumpa, N. A., Jones, C. P. & Robbins, P. E. (2009). *J. Phys. Conf. Ser.* **190**, 012039.

Diaz-Moreno, S., Amboage, M., Basham, M., Boada, R., Bricknell, N. E., Cibin, G., Cobb, T. M., Filik, J., Freeman, A., Geraki, K., Gianolio, D., Hayama, S., Ignatyev, K., Keenan, L., Mikulska, I., Mosselmans, J. F. W., Mudd, J. J. & Parry, S. A. (2018). *J. Synchrotron Rad.* **25**, 998–1009.

DuMond, J. W. M. (1937). *Phys. Rev.* **52**, 872–883.

Frahm, R., Griesebock, B., Richwin, M. & Lützenkirchen-Hecht, D. (2004). *AIP Conf. Proc.* **705**, 1411.

Frahm, R., Nachtegaal, M., Stötzel, J., Harfouche, M., Van Bokhoven, J. A. & Grunwaldt, J. D. (2010). *AIP Conf. Proc.* **1234**, 251.

Frahm, R., Richwin, M. & Lützenkirchen-Hecht, D. (2005). *Phys. Scr.* **2005**, 974.

Gaur, A., Shrivastava, B. D., Jha, S. N., Bhattacharyya, D. & Poswal, A. (2013). *Pramana J. Phys.* **80**, 159–171.

Hamzawy, A. (2016). *Radiat. Phys. Chem.* **119**, 103–108.

Jiang, D. T., Chen, N., Zhang, L., Malgorzata, K., Wright, G., Igarashi, R. & McKibben, M. (2007). *AIP Conf. Proc.* **882**, 893.

Kelly, J., Lee, T., Alcock, S. & Patel, H. (2013). *J. Phys. Conf. Ser.* **425**, 052009.

Khalid, S., Caliebe, W., Siddons, P., So, I., Clay, B., Lenhard, T., Hanson, J., Wang, Q., Frenkel, A. I., Marinkovic, N., Hould, N., Ginder-Vogel, M., Landrot, G. L., Sparks, D. L. & Ganjoo, A. (2010). *Rev. Sci. Instrum.* **81**, 015105.

Kirz, J. (2009). *X-ray Data Booklet*, edited by A. C. Thompson, pp. 3.1–3.4. Berkeley: Lawrence Berkeley National Laboratory. https://xdb.lbl.gov/Section3/Sec_3-1.html.

Klein, O. & Nishina, Y. (1929). *Z. Phys.* **52**, 853–868.

Klementiev, K., Norén, K., Carlson, S., Clauss, K. G. V. S. & Persson, I. (2016). *J. Phys. Conf. Ser.* **712**, 012023.

Kristiansen, P., Horbach, J., Döhrmann, R. & Heuer, J. (2015). *J. Synchrotron Rad.* **22**, 879–885.

Leshchev, D., Rakitin, M., Luvizotto, B., Kadyrov, R., Ravel, B., Attenkofer, K. & Stavitski, E. (2022). *J. Synchrotron Rad.* **29**, 1095–1106.

Mairs, T. R., Borrel, J. & Mathon, O. (2010). *DLS Proc.* **1**, e57.

Müller, O., Lützenkirchen-Hecht, D. & Frahm, R. (2015). *Rev. Sci. Instrum.* **86**, 093905.

Müller, O., Nachtegaal, M., Just, J., Lützenkirchen-Hecht, D. & Frahm, R. (2016). *J. Synchrotron Rad.* **23**, 260–266.

Pellicer-Porres, J., San Miguel, A. & Fontaine, A. (1998). *J. Synchrotron Rad.* **5**, 1250–1257.

Prestipino, C., Mathon, O., Hino, R., Beteva, A. & Pascarelli, S. (2011). *J. Synchrotron Rad.* **18**, 176–182.

Proux, O., Nassif, V., Prat, A., Ulrich, O., Lahera, E., Biquard, X., Menthonnex, J.-J. & Hazemann, J.-L. (2006). *J. Synchrotron Rad.* **13**, 59–68.

Rogers, C. S. & Assoufid, L. (1995). *Rev. Sci. Instrum.* **66**, 2200–2202.

Simonelli, L., Marini, C., Olszewski, W., vila Perez, M., Ramanan, N., Guilera, G. & Klementiev, K. (2016). *Cogent Phys.* **3**, 123198.

Solé, V. A., Gauthier, C., Goulon, J. & Natali, F. (1999). *J. Synchrotron Rad.* **6**, 174–175.

Stötzel, J., Lützenkirchen-Hecht, D., Fonda, E., De Oliveira, N., Briois, V. & Frahm, R. (2008). *Rev. Sci. Instrum.* **79**, 083107.

White, G. K. (1973). *J. Phys. D Appl. Phys.* **6**, 2070–2078.

Yang, B. X., Decker, G., Lee, S. H. & Den Hartog, P. (2010). *Proceedings of BIW10*, edited by C. Dillingham & J. Chew, pp. 233–237. Geneva: JACoW.

Zhang, L., Lee, W.-K., Wulff, M. & Eybert, L. (2003). *J. Synchrotron Rad.* **10**, 313–319.

Zhang, L., Sánchez del Río, M., Monaco, G., Detlefs, C., Roth, T., Chumakov, A. I. & Glatzel, P. (2013). *J. Synchrotron Rad.* **20**, 567–580.